JOURNAL OF MATERIALS SCIENCE 23 (1988) 3603–3611

The metallurgical structure of as-solidified Ni–Cr–B–Si–C hardfacing alloys

S. LEBAILI*, M. DURAND-CHARRE, S. HAMAR-THIBAULT
Institut National Polytechnique de Grenoble, L.T.C.M.-E.N.S.E.E.G, BP 75,
38402 St Martin d'Hères, France

The crystallization of complex nickel-base hardfacing alloys is studied with reference to the ternary Ni–Si–B and quaternary Ni–Cr–B–Si systems. Quenched interrupted, directional solidification is employed to establish the solidification sequence. The transformation temperatures are measured by differential thermal analysis. Solid-state transformations occurring during the cooling process are described. A model of the solute exchanges during solidification is proposed in order to predict the amount of liquid remaining at each stage in the process, particularly at the last stage when all the eutectic liquid is frozen in.

1. Introduction

One solution to many problems of wear and corrosion is the use of coatings. The deposit materials have to be chosen in relation to the deposit process, with the base material and with conditions of practical use. For many uses, a common requirement for the properties of coatings is a good corrosion resistance combined with an increased wear resistance. This requirement can be met by the use of the so-called "hardfacing alloys".

A family of these hard-facing alloys is constituted by nickel-base materials. Their structure is characterized by several phases such as carbides, borides and silicides formed with the base metal (nickel), and either a metallic (chromium, tungsten) or non-metallic (carbon, boron silicon) additive. A fine hard phase dispersion of hard precipitates is most beneficial with respect to wear resistance [1]. In spite of prolific literature on the subject, few papers deal with their microscopic metallurgical structure [2, 3]. Nevertheless, it is admitted that wear resistance is directly correlated to the microstructural features governing the interaction between the hard precipitates and the matrix: distribution, shape, coarseness and crystallographic orientation of the precipitates.

The presence of additional chromium gives the alloys good corrosion resistance and also raises the temperature stability by forming stable chromium carbides and borides. However, the boride phases are mainly responsible for the high hot hardness. One of the main features of these alloys is their autofluxing ability which may be attributed to boron. This property makes them interesting for the chemical and glass industries [4, 5]. In addition, silicon and boron lower the melting point and increase the solidification interval.

There is a great number of application methods based on a welding or spraying process. Hardfacing is usually performed with techniques involving a rather rapid solidification process such as plasma torch or electron bombardment. Consequently, some problems arise resulting from these particular conditions for solidification: for instance, the formation of non-equilibrium structures or the occurrence of solidification shrinkage.

The object of the present paper is not to optimize the composition of the alloys with regard to their hardfacing properties but to analyse the influence of the initial composition on the solidification process and on the resulting structure. Solidification is modelled by means of two parameters: the solidification range of temperature, ΔT, and the ratio liquid/liquid + solid, f_L, during the freezing process. In the case of our alloys, the amount of eutectic liquid remaining at the end of solidification is large. This facilitates the spreading of the liquid layer and governs the final aspect of the deposit. The two parameters, ΔT and f_L, depend on the phase diagram, then on the crystallization path and on the solidification conditions.

In order to establish the solidification sequences, the quench interrupted directional solidification technique seems well adapted. We propose to study in this way some commercial alloys and to establish a comparison with less complex synthetic alloys.

2. Experimental procedure

Master alloys were prepared under a controlled atmosphere using pure (99.9%) charge materials. Intermediate compositions were prepared from these alloys by button melting in an argon arc furnace equipped with a non-consumable tungsten electrode. In all, a total of six synthetic alloys were studied in the composition range, 0 to 15 wt % B, 0 to 19 wt % Si, and five commercial alloys. The compositions are indicated in Table I and the points representing them are reported in Fig. 1.

The temperatures of phase transformation were

---

*Present address: Commissariat aux Energies Nouvelles; 2 brd Frantz Fanon, Alger, Algeria.

0022–2461/88 $03.00 + .12

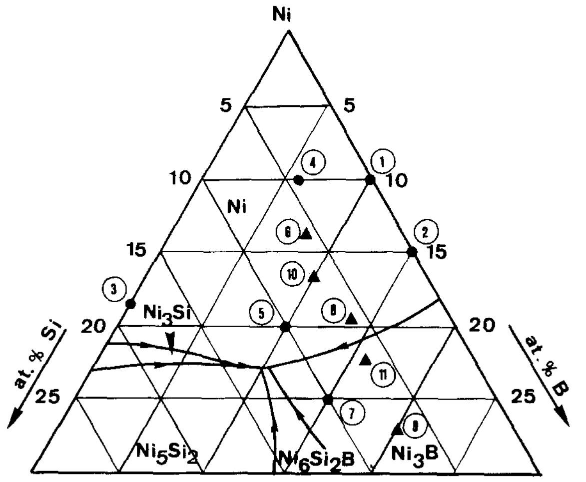

Figure 1 Liquidus projection for the system Ni–B–Si. For complex commercial alloys (*) indicated by a triangle in the figure, chromium and other element contents were included with nickel.

determined by differential thermal analysis (DTA) on specimens of about 2 g. Heating and cooling were carried out under argon at a rate of 5° C min^{-1}.

Some specimens of commercial alloys were examined after quench interrupted directional solidification (QIDS). The method consists of monitoring solidification under controlled conditions of thermal gradient and rate of advance of the solid–liquid interface. The specimens were elongated bars, 23 cm long and 0.8 cm diameter. The bars are drawn from the hot zone of a high-frequency furnace to the cold zone of a water jacket. Steady-state conditions are established and the rate of advance of the interface may be assimilated to the forward movement of the bar, i.e. in this case 18 cm h^{-1}. The plot of temperatures in the furnace is shown in Fig. 2. The thermal gradient in the solid varies from 600° C near the interface at the liquidus temperature to 40° C cm^{-1} at a distance of about 3 cm where the temperature is 800° C. Quenching froze in the interface configuration and also the evolution of the solidified alloy when passing through the hot zone. Examination of the structures along the bar enables the solidification sequence to be determined and the solid state transformations to be detected.

Optical micrographs were taken on polished sections etched in Murakami or Villela reagent. Identification of the phases was confirmed by X-ray diffraction using filtered copper radiation ($K\alpha$ = 0.1541 nm), particularly in the case of the hard phase extracted by dissolution of the matrix. The examination of the microstructure with a scanning electron microscope (SEM-JSM35) were carried out on samples chemically etched with a solution of $FeCl_3$ in HCl which slightly dissolves the matrix. Electron probe analysis was carried out using a Cameca MS46 and subsequent application of a ZAF correction program (atomic number, absorption and fluorescence).

More accurate observations were made by transmission electron microscopy (TEM) with a JEM200CX. Electropolishing of the thin foils was done with an electrolyte solution of 13% HCl in methyl alcohol at −40° C.

3. Results

3.1. Microstructural observations

The phases observed in most of the alloys are: Ni(α) solid solution, M_7C_3-type chromium carbides, CrB and Ni_3B chromium and nickel borides, Ni_5Si_2 nickel silicides. Their crystallographic structures are indicated on Table II [6–9]. QIDS was operated on some commercial alloys [10]. The results concerning 6* and 8* are presented. Alloy 6* is representative of hypoeutectic compositions in the Ni(α) primary field. Alloy 8*, on the other hand, is representative of those alloys having as first phase an intermetallic compound CrB in this case. Figs 2 and 3 illustrate the morphologies of the primary phases and of all the phases formed during the solidification sequence.

Fig. 2 shows electron micrographs for alloy 6* specimens taken along the solidified rod. At the top of the rod the Ni(α) dendrites may be easily distinguished from the quenched liquid. In the case of dendrites quenched at the early stage of their formation, the secondary arms are well developed. As the freezing rate is rather slow, the interspacing of the primary axes is large (≈ 100 μm). At high temperature, diffusion is very effective and promotes a coarsening process. Then, in the mushy zone, dendrites break into small, round shaped pieces. Each stage of solidification defines a macroscopic interface on the rod, indicated by an arrow on Fig. 2. Figs 2a and b show the electron micrographs of the magnified areas corresponding, respectively, to the eutectic structures Ni(α)/Ni_3B and Ni_3B/Ni_5Si_2. Fig. 3 shows

TABLE I Transformation temperatures and phases formed for each alloy in the order of their appearance. The alloys labelled * are commercial alloys

Alloy	Cr (at. %)	B (at. %)	Si (at. %)	C (at. %)	Transition temperatures (° C)	Phases in order of appearance
1	–	10	–	–	1280 1095	Ni(α) Ni_3B
2	–	15	–	–	1185 1095	Ni(α) Ni_3B
3	–	–	19	–	1225 1160 1125 1008	Ni(α) Ni_5Si_2
4	–	6	4.5	–	1275 915 885	Ni(α) Ni_3B
5	–	10	10	–	1120 1030 985	Ni(α) Ni_3B Ni_5Si_2
6*	7.5	8	6.3	1	1175 975 985	Ni(α) Ni_3B Ni_5Si_2
7	–	15	10	–	1030 1010 1000 985	Ni_3B Ni_6Si_2B Ni
8*	14	14	6.3	1.5	1025 990 955	CrB Ni M_7C_3 Ni_3B Ni_5Si_2
9*	11	20	8	1.5	1040 960 940	CrB Ni M_7C_3 Ni_3B Ni_5Si_2
10*	10	10	7	2	1075 976 955	M_7C_3 Ni Ni_3B Ni_5Si_2
11*	15	17	7	3.6	1030 970 948 933	M_7C_3 Ni Ni_3B Ni_5Si_2

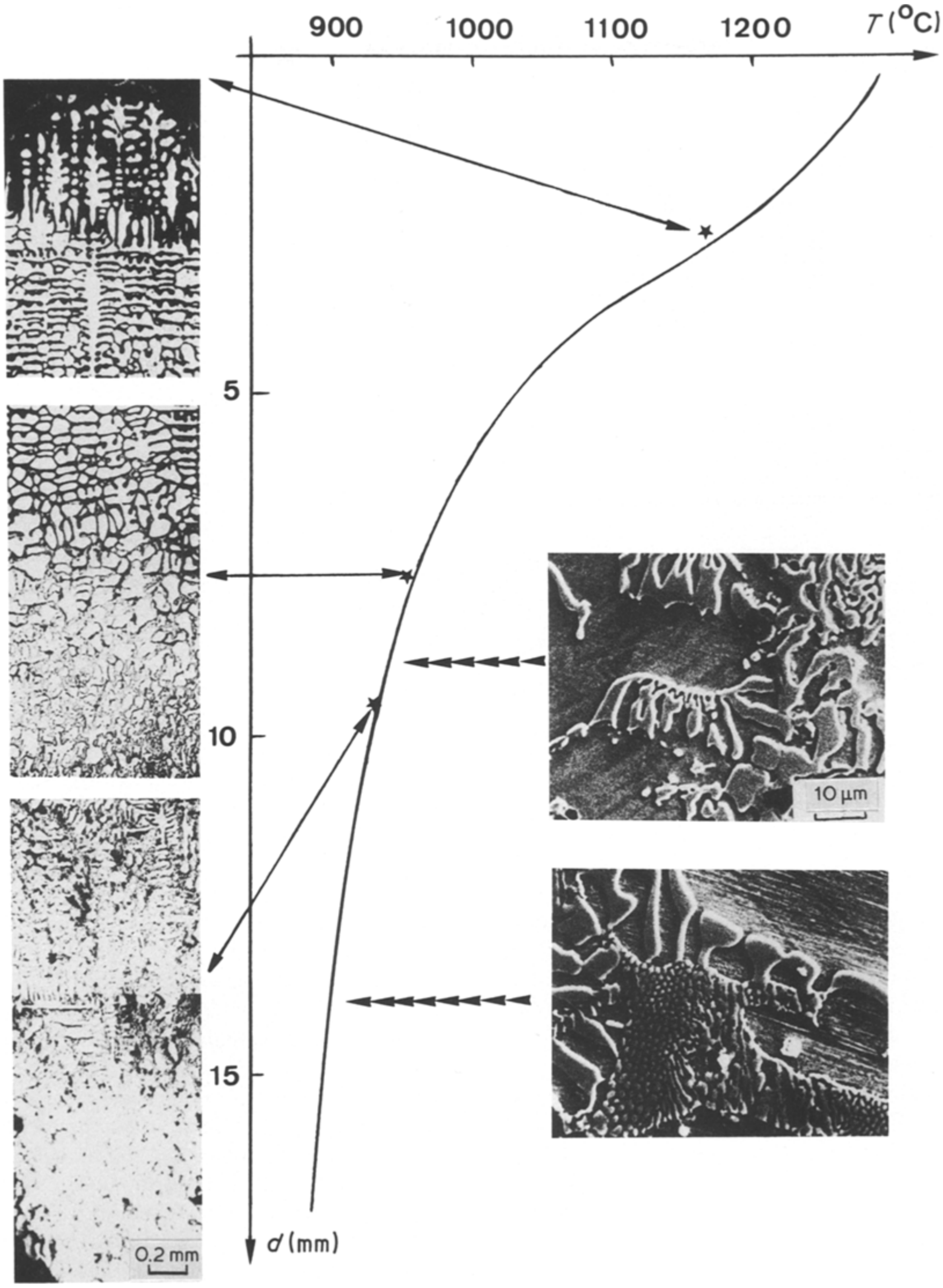

Figure 2 Secondary electron micrographs of alloy 6*. The plots represent the temperature profile in the bar during the unidirectional solidification process. The arrows indicate the temperature of the specimens corresponding to the micrographs just before quenching. On the left hand are longitudinal cuts, on the right hand two magnified areas of transversal cuts (a) Ni(α)/Ni_3B eutectic; (b) Ni_3B/Ni_5Si_2 eutectic.

TABLE II Crystallographic structures and lattice parameters of the phases identified

Compound	Space Group	Lattice Parameter (A)			References
		a	b	c	
Ni	Fm3m	3.52			[8]
Ni_3B	Pbnm	4.389	5.211	6.619	[8]
Ni_2B	14cm/m	4.99		4.26	[8]
$Ni_3Si\beta1$	L12	3.51			[8]
$Ni_3Si\beta2$	monoclinic	7.04	6.24	5.08	[7]
$Ni_3Si\beta3$	Pbnm	4.35	5.50	6.50	[6]
Ni_5Si_2	P3h	6.66		12.27	[8]
Ni_6Si_2B	P62m	6.10		2.89	[11]
CrB	C2/mcm	2.97	7.86	2.93	[8]
M_7C_3	C43v	13.98		4.52	[8]

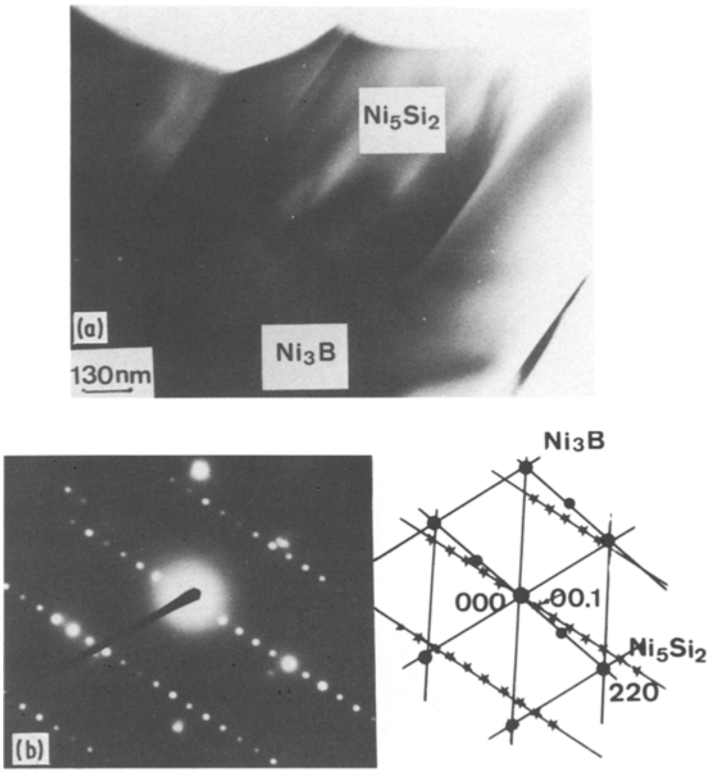

Figure 3 (a) Transmission electron micrograph of Ni_3B/Ni_5Si_2 eutectic; (b) corresponding key diagram.

transmission electron micrographs of this later eutectic. The phases are indexed as orthorhombic Ni_3B and hexagonal Ni_5Si_2. We observe that the (0 0 0 1) plane for Ni_5Si_2 is very close to the (0 2 2) plane for Ni_3B, though no orientation relationship can be really defined.

In Fig. 4, the primary CrB dendrites appear quite different, rather blocky. Beside them, Ni(α) dendrites can be observed. They are well formed with secondary and even tertiary arms. It can be noticed that they are very thin and do not coarsen like the preceding ones. Fig. 4b presents the eutectic Ni(α)/CrB and the eutectic boride appears with a coarsened, round-shaped morphology. Fig. 4c shows two transitory structures: the top one is a ternary eutectic Ni(α)/M_7C_3/CrB, the bottom one is Ni(α)/Ni_3B. Fig. 4d corresponds to the ternary Ni(α)/Ni_3B/Ni_5Si_2 eutectic. This last ternary eutectic represents a small volume fraction of the alloy and its solidification is achieved in a narrow temperature range. As a result the microstructure is very fine.

Fig. 5 also shows electron micrographs of DTA specimens of alloys 8* and 10* illustrating the facetted morphologies of primary intermetallic compounds CrB and M_7C_3. Chromium carbides exhibit their typical facetted, spade-like morphology. However, on account of the slow freezing rate, the features of the morphologies are more characteristic and easier to analyse in the QDTA specimens.

3.2. Solidification sequences

The crystallization paths are defined by two kinds of data: the transition temperatures resulting from DTA experiments and the order of appearance of the phases. Both are indicated in Table I for all the alloys, synthetic or commercial (labelled by *). The phase which first solidifies depends on the composition of the initial alloys. For the ternary system Ni–Si–B, the extent of the primary fields is shown on the liquidus projection in the nickel-rich corner established by Lebaili *et al.* [11] (Fig. 1). All the compositions investigated in the present study have been reported on this projection taking into account only the amount of boron and silicon. This rough approximation assumes that chromium is found only in the matrix and that other element contents may be neglected. In fact, for commercial alloys, the primary phase is different from that expected. Alloys 10* and 11*, with a rather high carbon content and high chromium content (respectively 2 to 3.6 wt % C and 10 to 15 wt % Cr), form M_7C_3 carbides as primary phase. Alloys 8* and 9* form CrB. Alloy 6*, with lower carbon and chromium contents than the preceding ones, belongs to the primary Ni(α) phase field of the quarternary system.

However, the sequences of solidification mentioned on Table I for all the compositions are rather similar. The crystallization of alloy 7 finishes at 985° C at an invariant point corresponding to the ternary eutectic transformation between Ni(α), Ni_3B and Ni_6Si_2B [11]. The temperatures of the end of crystallization are close for alloys 5 and 6. In effect, the alloys presenting a thermal accident on thermograms ranging between 980 and 990° C exhibit a large amount of Ni(α)/Ni_3B eutectic and a smaller amount of Ni(α)/Ni_3B/Ni_5Si_2 eutectic. In the case of chromium-containing alloys, a similar accident, in a lower temperature range (940 to 955° C), was associated with the formation of a different ternary eutectic Ni(α)/Ni_3B/Ni_5Si_2 following the formation of Ni(α)/Ni_3B eutectic (alloys 8*, 9*, 10* and 11*) or Ni_3B/Ni_5Si_2B eutectic (alloy 6*). The crystallization of alloy 11*, which contains the largest amount of carbon and chromium, begins by the formation of M_7C_3 carbides and terminates also by the formation of the same ternary eutectic Ni(α)/Ni_3B/Ni_5Si_2 at 935° C.

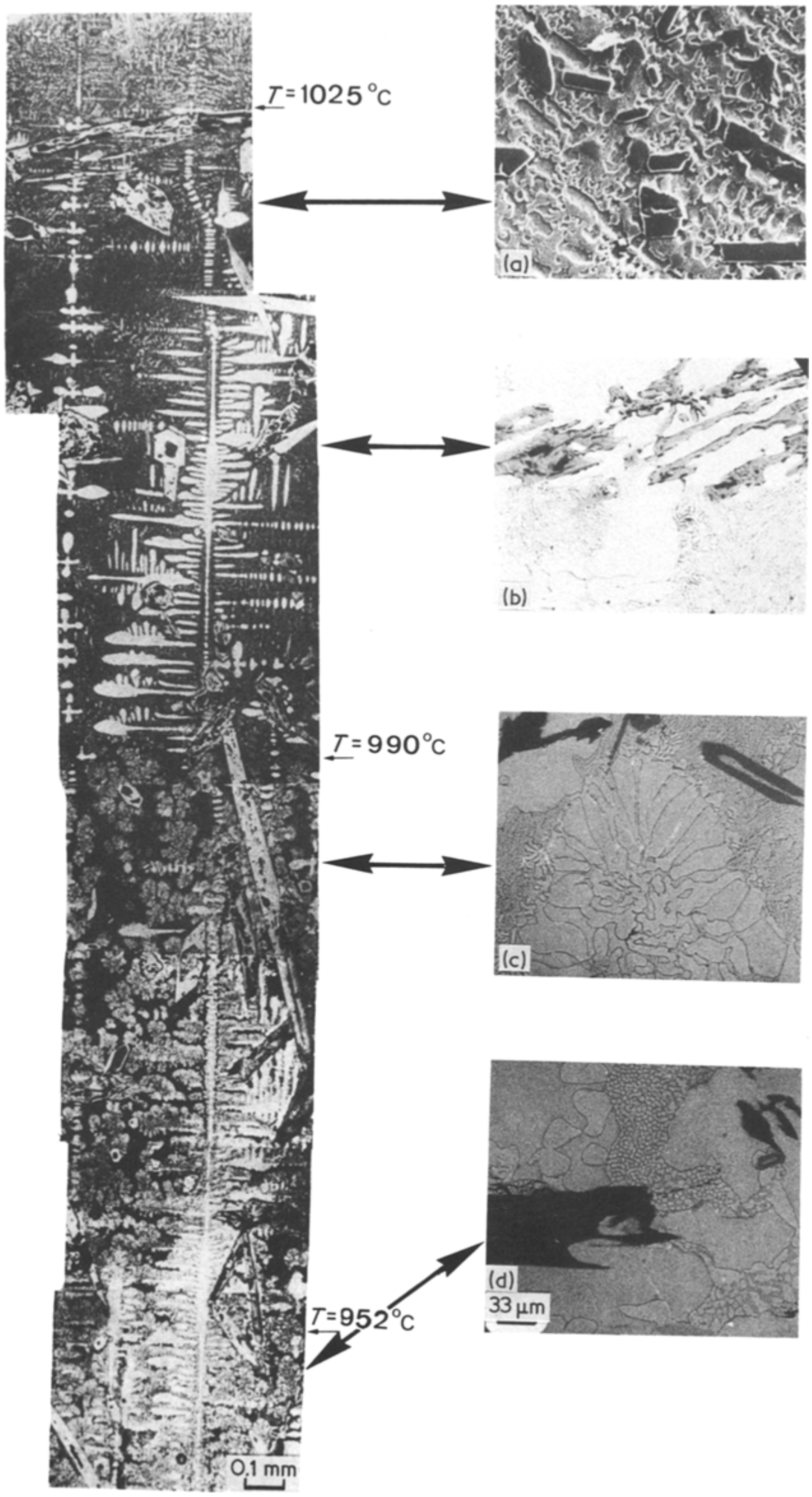

Figure 4 Secondary electron micrographs of alloy 8*. The magnified areas correspond to: (a) primary CrB; (b) Ni(α)/CrB eutectic; (c) top, Ni(α)/M_7C_3/CrB; bottom, Ni(α)/Ni_3B; (d) Ni(α)/Ni_3B/Ni_5Si_2.

We have reported in Table III the results of microprobe analyses, in the case of alloy 9*, with the mention of the range of composition of each compound. For all the phases, except M_7C_3, there is little variation of composition related to the thermal history. In the case of M_7C_3 carbide, we measured a lower nickel content (4 at.%) for carbides occurring as the primary phase than for those occurring as the eutectic phase (8 at. %).

Considering the use of this type of alloy, we have determined two parameters in order to describe the cooling process: the solidification interval and the amount of liquid phase remaining in the interdendritic groove when the first eutectic structure forms. The interval of solidification is indicated in Table I and lies between 50 and 200° C. The liquid fraction or the complementary solid fraction were estimated by examination of the micrographs of quenched specimens (Table IV).

TABLE III Composition of the phases identified in alloy 9*

	CrB (at %)	Ni_5Si_2 (at %)	Ni_3B (at %)	M_7C_3 (at %)
Ni	0.4	93.2	69.4	4.1
Cr	49.9	0.4	6.1	65.4
B	49.6	0	24.5	0
Si	0	26.4	0.1	< 0.1
C	0	0	0	29.5

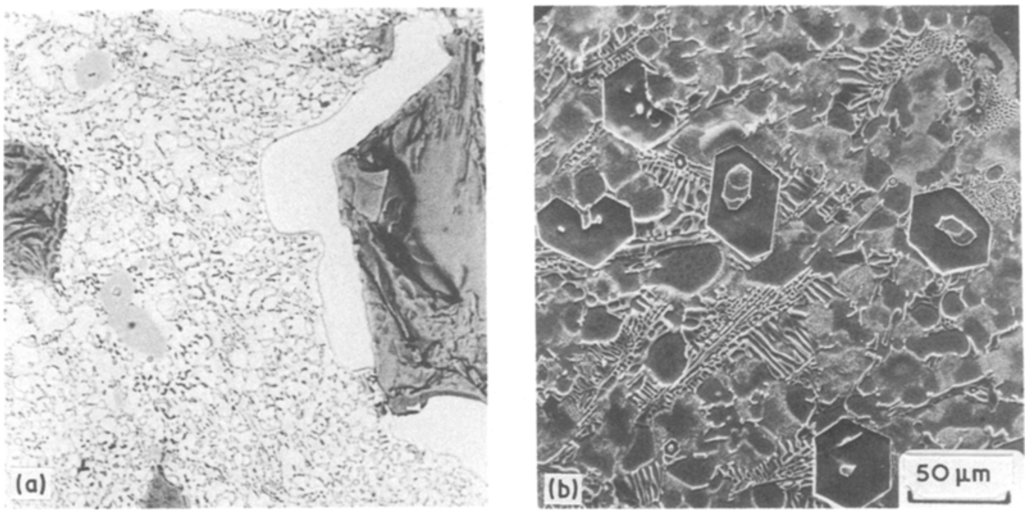

Figure 5 Secondary electron micrographs illustrating the primary blocky phases: (a) CrB in alloy 8*; (b) M_7C_3 in alloy 10*.

3.3. Solid-state precipitation

During the cooling process, precipitates appear at different temperatures in the Ni(α) dendrites (Fig. 6). These precipitates were identified as $\beta 1 Ni_3Si$ (Table II). Other structures labelled β2 and β3 were not observed. In fact the latter two are only observed for the binary system in alloys aged at high temperature for a relatively long time [6].

The precipitates are located on the border of the dendrites. This fact can be related to the large variation in silicon content between the border and the centre of the dendrites due to solidification segregation. For example, in alloy 5, the silicon content may reach 11 at. % at the border, which is 6 at. % higher than in the centre. We distinguished two morphologies for these precipitates: a cuboid one with faces parallel to (1 0 0) planes (Fig. 6) and a dendritic one (Fig. 7b). These latter precipitates were observed in alloy 8* (Fig. 4) at the bottom of the bar of QIDS specimens. The analyses of the precipitates did not indicate any substitution of nickel or silicon by chromium. Fig. 6 presents a STEM qualitative analysis; no chromium X-peak could be detected.

Chromium prevents the formation of the primary phase Ni_6Si_2B. This phase was found only in chromium-less alloys and then it is not stable. It decomposes during slow cooling or ageing, giving Ni_3B and Ni_5Si_2.

4. Discussion and conclusions

This discussion will be focused particularly on two points:

(i) the structural features related either to the initial composition of the alloy or the parameters of the freezing and cooling processes,

(ii) modelling of solute exchanges during solidification in order to predict the amount of liquid remaining at each stage in the process.

TABLE IV Fraction solidified f_s before the formation of the eutectic structure. The calculated values and the values estimated by quantitative metallography are given for ternary alloys and alloy 6*

Alloy	ΔT	f_s measured	f_s calculated
1	185	0.50	0.46
2	90	0.25	0.22
3	217	0.35	0.50
4	290	0.60	0.68
5	135	0.12	0.20
6*	190	0.33	0.50

4.1. Metallurgical structure and morphology

The crystallization paths are very complex for commercial alloys. Several eutectic structures with intermetallic compounds may be found. However, they may be predicted by comparison with the ternary model system Ni–Si–B. In the case of chromium-containing alloys, modifications have to be taken into account.

Chromium promotes the formation of CrB as primary phase when its content exceeds about 10 wt %. For chromium- and boron-rich alloys the primary phase is always CrB. For alloys containing chromium, boron and carbon, there is competition between boron and carbon for the formation of either borides or carbides. This fact was established by Pradelli [12] in the case of the ternary system Cr–C–B. Our previous work [13] concerning the quarternary system Ni–Cr–C–B shows the influence of nickel addition. A projection of the liquidus surface is proposed for the system $(Ni_{0.66}, Cr_{0.33})$–C–B (Fig. 8). The extent of the Cr_2B primary field is not as large as that of the ternary system. In fact Cr_2B could be detected only for alloys of composition very close to that of the binary eutectic Ni(α)/Cr_2B. The field of the ternary compound Ni_6Si_2B is also reduced; it disappears for a chromium content of about 2%. There is a monovariant line between Ni_3B and Ni_5Si_2 that reaches the ternary eutectic. With a carbon content higher than 2 wt %, M_7C_3 occurs almost independently of the boron content.

The $\beta 1 Ni_3Si$ precipitates exhibit the two characteristic morphologies for this kind of $L1_2$ precipitate coherent with the Ni(α) matrix: cuboids and dendrites, as presented in Figs 6 and 7. The faces of the cuboids are parallel to the (1 0 0) planes. The growth directions for dendritic $\beta 1 Ni_3Si$ are the ⟨1 1 1⟩ directions of the Ni(α) matrix. The occurrence of such precipitation has been widely investigated in the case of γ′ (Ni_3Al)

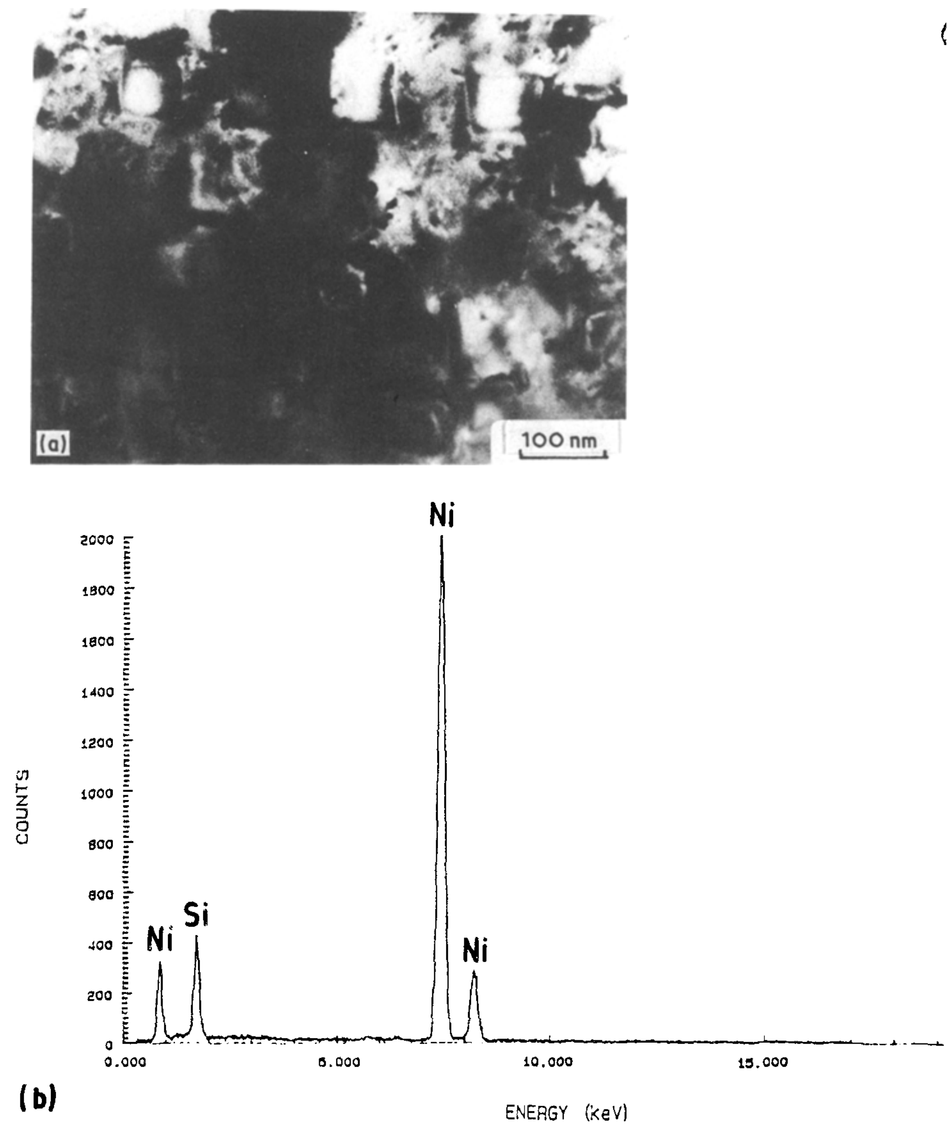

Figure 6 (a) Transmission electron micrograph for alloy 6* showing solid- state precipitation; (b) X-ray analysis of $\beta 1 \mathrm{Ni_3Si}$ precipitates.

precipitates in a nickel matrix because it constitutes the strengthening mode for superalloys. These two morphologies are also observed in the Ni–Si binary alloy 3 and in the more complex commercial alloy 8* [6, 14]. For superalloys, many interpretations have been suggested for the occurrence of one specific morphology. For Ricks *et al.* [15] the morphologies are correlated with two parameters: the sign of the lattice misfit between the matrix and the precipitates, and the supersaturation of the diffusing species. In fact, the lattice misfit is very small and consequently accurate measurements are difficult to carry out. Again, the misfit depends on temperature and may be different at the precipitation temperature from that measured at

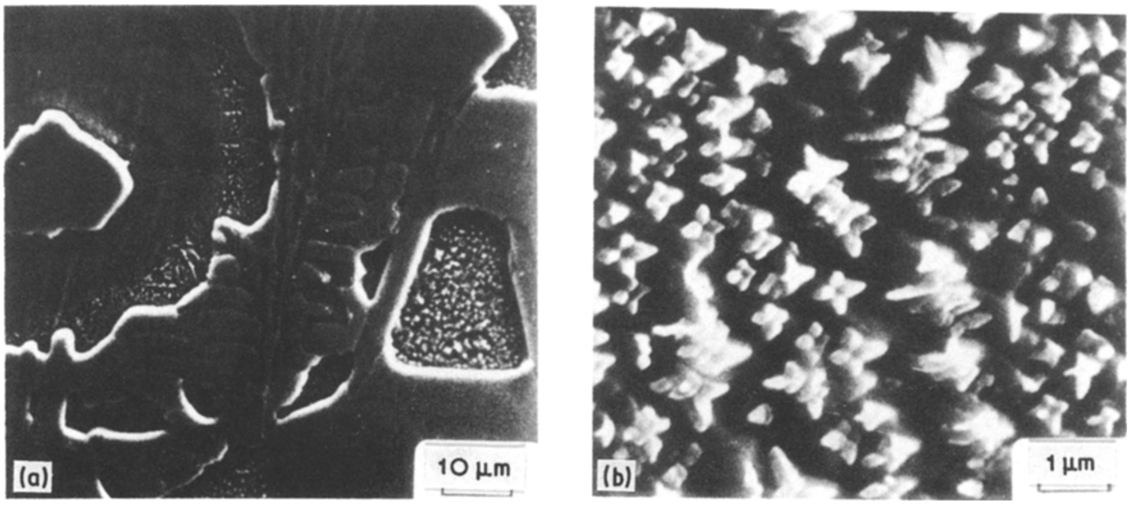

Figure 7 Electron micrographs illustrating dendritic solid state precipitation in alloy 8*. The specimen has been unidirectionally solidified and slowly cooled.

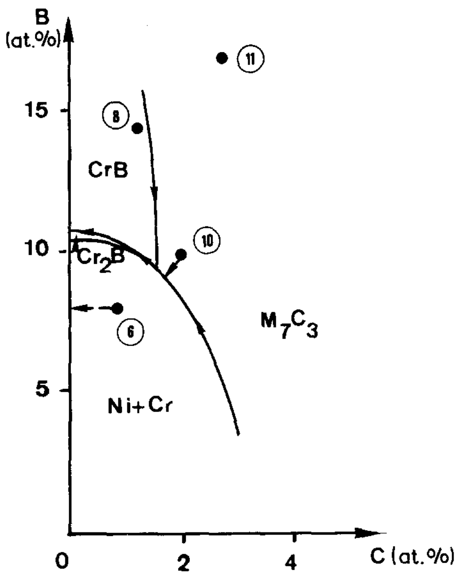

Figure 8 Projection of the polyphased lines in the system (Ni, Cr)–CrB for a content of 66 at. % Ni; taken from [13].

room temperature. The effect of supersaturation involves a kinetic effect related to the phase diagram. Some authors have shown the evolution of cuboid precipitates into dendritic precipitation and explained it by the growth along preferential planes.

4.2. Modelling of solute exchanges

The achievement of a solidification process involves solute exchanges which depend, on the one hand, on the solid–liquid equilibria and, on the other hand, on kinetic aspects. In order to describe these exchanges, several relationships have been established. The lever rule expresses the partitioning of an element when an equilibrium state is reached. The Scheil (or Gulliver) law expresses the equilibrium at the liquid–solid interface with the assumptions that there is no diffusion in the solid phase and that the liquid phase is completely homogeneous. This law was adapted to the dendrite scale [16] to calculate the solute enrichment in the interdendritic groove. Other more realistic models have been proposed which take into account partial diffusivity of solute into the solid phase [17]. The necessary thermodynamical data are: the partition coefficient k for each solute and the diffusion coefficients D in the solid phase. Our purpose is to calculate the composition of the phase at each step in the solidification process represented by the remaining liquid fraction. Assuming that the partition coefficients are constant and that ternary interaction between solutes may be neglected, we did a numerical treatment of equations given in the Appendix. For silicon, the value of the partition coefficient that we have taken is 0.78 which is the value in the Ni–Si system at the eutectic composition. For boron, the partition coefficient is very small (0.08) because boron is not very soluble in nickel. We carried out the calculations using the lever rule for boron and the Scheil rule for silicon. As the diffusivity of boron is very high at these temperatures, equilibrium can be reached readily for this element and the use of the lever rule is justified.

Fig. 9 presents the results reported on the liquidus projection. The amount of liquid, f_L, remaining after solidification of primary dendrite, f_s, is indicated according to the range of composition. The primary Ni(α) field is divided into two parts; one for which the solidification process is achieved by the formation of Ni(α)/Ni_5Si_2 eutectic and another one by the formation of Ni(α)/Ni_3B eutectic.

More sophisticated calculations were carried out, taking into account back-diffusion of silicon in the solid but resulted in little difference for the crystallization paths. This is due to the very small partition coefficient of boron which leads to paths nearly parallel to the boron axis. The amount of remaining liquid, f_L, is modified by back diffusion of silicon when the interval of solidification, ΔT, is large and the soldification rate rather slow. The modification is significant only for compositions above the line $f_L = 0.60$. Indeed, quantitative metallographic estimations for f_s indicated in Table IV are in rather good agreement with the predicted values when ΔT is not too large.

Appendix

The relationships involved in the numerical treatment are:

$$\text{Scheil's law} \quad \frac{\mathrm{d}X_{Si}}{X_{Si}} = (1 - k_{Si})\left(\frac{\mathrm{d}f_L}{f_L}\right) \qquad \text{(A1)}$$

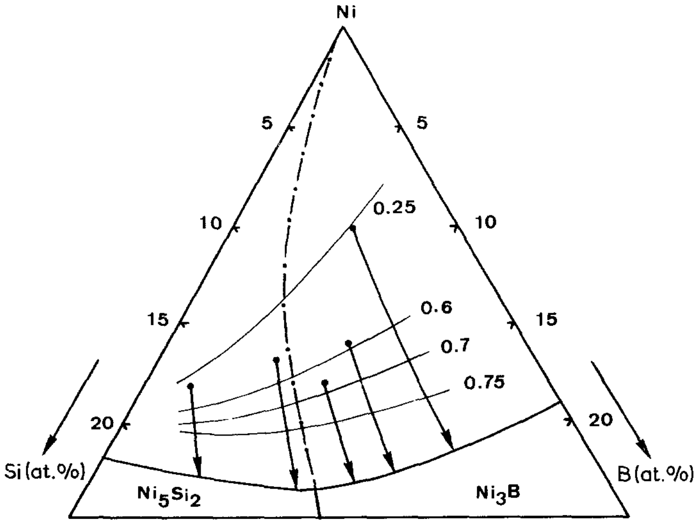

Figure 9 Proportion of liquid, f_L, remaining at the end of primary solidification as a function of initial composition. The isoproportion lines are reported on the projection of the liquidus surface. The dotted line separates the field to show that the crystallization path ends by the formation of different eutectic structures.

$$\text{lever rule} \quad \frac{\mathrm{d}X_{\mathrm{B}}}{X_{\mathrm{B}}} = \frac{(1 - k_{\mathrm{B}})\mathrm{d}f_{\mathrm{L}} + (1 - f_{\mathrm{L}})\mathrm{d}k_{\mathrm{B}}}{f_{\mathrm{L}} + (1 - f_{\mathrm{L}})k_{\mathrm{B}}} \tag{A2}$$

the partition coefficients k_{B} and k_{Si} are assumed constant: $k_{\mathrm{B}} = 0.08$; $k_{\mathrm{Si}} = 0.78 = 1$ to 0 (III) $f_{\mathrm{L}} = 0.02$ for each step, where f_{L} is the liquid fraction.

References

1. O. KNOTEK, E. LUGSCHEIDER and H. REIMAN, "Metallurgical Aspects of Wear" (Deutsche Gesellshaft für Metallkunde, Oberursel, 1981).
2. H. T. STEINE and W. SIMM, *Int. J. Powder Metall. Powder Technol.* **18** (1982) 57.
3. YU. P. OSHCHEPKOV and N. V. OSHCHEPKOV, *Met. Sci. Heat Treat.* **21** (1979) 755.
4. O. KNOTEK, E. LUGSCHEIDER and H. REIMANN, *J. Vac. Sci. Technol.* **12** (1975) 770.
5. P. V. GLADKI, E. F. PEREPLETCHIKOV and I. I. FRUMIN, *Avt. Svarka* **21** (9) (1968) 58.
6. S. LEBAILI and S. HAMAR-THIBAULT, *Z. Metallkde.* **75** (1984) 764.
7. R. P. RAM and S. BHAN, *ibid.* **66** (1975) 521.
8. M. HANSEN and K. ANDERKO, "The constitution of binary alloys" (McGraw-Hill, New York, 1958).
9. E. LUGSCHEIDER, H. REIMAN and U. KNOTEK, *Monatsheft Chemie* **106** (1975) 1155.
10. S. LEBAILI, Thèse Docteur-Ingénieur, INP-Grenoble (1984).
11. S. LEBAILI and S. HAMAR-THIBAULT, *Acta Metall.* **30** (1987) 501.
12. G. PRADELLI, *Metall. italiana* **70** (1978) 223.
13. S. LEBAILI and S. HAMAR-THIBAULT, *Mém Sci. Rev. Metall.* (1984) 519.
14. G. S. GARDINER, J. HUMMEL, M. A. RAHNEMA, M. A. RUGGEIRO and J. W. RUTTER, *J. Crystal Growth* **58** (1982) 522.
15. R. A. RICKS, A. J. PORTER and B. C. ECOB, *Acta Metall.* **31** (1983) 43.
16. T. F. BOWER, H. D. BRODY and M. C. FLEMINGS, *Trans. AIME* **236** (1966) 624.
17. T. W. CLYNE and W. KURZ, *Met. Trans.* **12A** (1981) 965.

*Received 14 July
and accepted 9 October 1987*